Available online at www.sciencedirect.com
ScienceDirect
Acta Biomaterialia 4 (2008) 490–503
Acta BIOMATERIALIA
www.elsevier.com/locate/actabiomat

Characterization of mineralized collagen–glycosaminoglycan scaffolds for bone regeneration

Biraja P. Kanungo [a], Emilio Silva [b], Krystyn Van Vliet [a], Lorna J. Gibson [a,*]

[a] Department of Materials Science and Engineering, Massachusetts Institute of Technology, Cambridge, MA 02139, USA
[b] Department of Civil and Environmental Engineering, Massachusetts Institute of Technology, Cambridge, MA 02139, USA

Received 21 August 2007; received in revised form 28 November 2007; accepted 4 January 2008
Available online 26 January 2008

Abstract

Mineralized collagen–glycosaminoglycan scaffolds designed for bone regeneration have been synthesized via triple co-precipitation in the absence of a titrant phase. Here, we characterize the microstructural and mechanical properties of these newly developed scaffolds with 50 and 75 wt.% mineral content. The 50 wt.% scaffold had an equiaxed pore structure with isotropic mechanical properties and a Ca–P-rich mineral phase comprised of brushite; the 75 wt.% scaffold had a bilayer structure with a pore size varying in the through-thickness direction and a mineral phase comprised of 67% brushite and 33 wt.% monetite. The compressive stress–strain response of the scaffolds was characteristic of low-density open-cell foams with distinct linear elastic, collapse plateau and densification regimes. The elastic modulus and strength of individual struts within the scaffolds were measured using an atomic force microscopy cantilevered beam-bending technique and compared with the composite response under indentation and unconfined compression. Cellular solids models, using the measured strut properties, overestimated the overall mechanical properties for the scaffolds; the discrepancy arises from defects such as disconnected pore walls within the scaffold. As the scaffold stiffness and strength decreased with increasing overall mineral content and were less than that of natural, mineralized collagen scaffolds, these microstructural/mechanical relations will be used to further improve scaffold design for bone regeneration applications.

Keywords: Mineralized scaffolds; Collagen; Mechanical characterization; Microstructural characterization; Cellular solids model

1. Introduction

Scaffolds for tissue regeneration are defined as: "three-dimensional open-cell porous structures synthesized from either natural or synthetic polymers which have the potential to support attachment, migration and multiplication of living cells" [1]. These structural mimics of the extracellular matrix can be made of biodegradable synthetic polymers (e.g. polylactic and polyglycolic acid) or natural polymers (e.g. collagen, collagen–glycosaminoglycan copolymer). It has been demonstrated that scaffold pore size and shape, porosity, specific surface area, biodegradability and stiffness significantly influence cell functions [2]. To control these features, various fabrication techniques have been developed for different biomaterials. For instance, synthetic polymer scaffolds can be made by negative mold infiltration, ceramic scaffolds can be made by a casting and sintering operation and collagen scaffolds are formed by freeze-drying (described in more detail below). Recently, attempts have been made to regenerate bone using synthetic [3–8] as well as natural polymer scaffolds [9–18].

Bone is comprised principally of the fibrous protein collagen (type I) [19,20], impregnated with a mineral closely resembling hydroxyapatite, $Ca_{10}(PO_4)_6(OH)_2$; it also contains non-collagenous proteins and water. The bone mineral is impure and has many structural substitutes (e.g. carbonate, fluoride and citrate); crystals are initially precipitated between and within the layers of collagen molecules [19,20]. Living cells (osteocytes, osteoblasts and

* Corresponding author. Tel.: +1 617 253 2503; fax: +1 617 253 8388.
E-mail address: ljgibson@mit.edu (L.J. Gibson).

1742-7061/$ - see front matter © 2008 Acta Materialia Inc. Published by Elsevier Ltd. All rights reserved.
doi:10.1016/j.actbio.2008.01.003

osteoclasts) populate within the vascularized extracellular matrix. The Young's modulus of wet cancellous bone ranges from 0.09 to 1.0 GPa, while that of wet cortical bone ranges from 10 to 20 GPa, depending on the direction of loading. The relative density (the density of the cellular solid, ρ^*, divided by that of the solid from which it is made, ρ_S) of cancellous bone ranges from 0.05 to 0.6 [19,20].

To optimize the regenerative capability of a scaffold, it is generally believed that the composition and physical/mechanical properties of the scaffold should be similar to those of the physiological extracellular matrix [21–26]. To this end, over the past decade collagen–glycosaminoglycan (CG) scaffolds have been developed and used clinically for skin regeneration and experimentally for nerve regeneration [21–25,27–32]. CG scaffolds are primarily manufactured through a freeze-drying process. Briefly, an aqueous CG slurry suspension is frozen to obtain interconnected ice crystals of the required size and shape. Sublimation of the frozen slurry leaves behind a foam-like network of struts with interconnected pores. Subsequently, the scaffolds are cross-linked to obtain the required mechanical properties and biodegradability. Extensive mechanical characterization of CG scaffolds has been reported by Harley et al. [27]. To mimic natural bone tissue, a mineral phase similar to hydroxyapatite must be added to the CG scaffold. A major area of recent progress has been the fabrication of mineralized bio-organic composites [33–38]. Most of these processes include mechanical mixing of the desired amount of monolithic calcium phosphate with the bio-organics. The major problem with these methods is that the mineral phase does not form in situ and simply adheres to the outside of the collagen [39–43]. This creates two shortcomings: the scaffold does not mimic bone, which has mineral dispersed throughout the collagen fibers; and, as the scaffold is resorbed by cells in the body, the outer mineralized layer of the scaffold is resorbed first, leaving unmineralized collagen scaffold struts. Other techniques yield in situ formation of calcium phosphate on the bio-organic component by adjusting the pH via a titrant phase [44–46]. However, these techniques have difficulty in controlling the mass yield of mineral phase as well as in removing the residual titrant phase, which can be harmful to cells. The most recent fabrication technique, developed by Lynn et al. [9,11,12,14,16–18], improves upon this mineralization process by forming a triple co-precipitate of mineral, collagen and glycosaminoglycan, without using a titrant, by controlling the molarity of the reactant acid and molar ratios of the different calcium sources. Due to the in situ co-precipitation of the mineral phase, calcium phosphate crystals form within the collagen fibers, resulting in a more uniformly mineralized scaffold that more closely resembles bone [9,11,12,14]. Freeze-drying is then used to fabricate porous scaffolds from the triple co-precipitated slurry.

Scaffolds with well-characterized and controllable chemical, mechanical and micro-structural properties are also suitable for basic in vitro studies of cell interactions. However, extensive characterization of these newly developed mineralized collagen–glycosaminoglycan (MCG) scaffolds has not yet been done. In this study, we fabricate MCG scaffolds with varying mineral contents via the triple co-precipitation method and characterize their microstructure as well as their mechanical properties. The mechanical properties of these mineralized scaffolds are discussed in light of the cellular solids models for porous open-cell foams. The mechanical properties were found to be less than those of scaffolds made by previous techniques, as well as those predicted by theoretical models, suggesting that their properties could be improved. In the future, we plan to modify the process used to make our scaffolds in order to improve their mechanical properties [4].

2. Materials and methods

2.1. Fabrication of MCG scaffolds

MCG scaffolds were fabricated using microfibrillar, type-I collagen isolated from bovine tendon (Integra LifeSciences, Plainsboro, NJ), chondroitin-6-sulfate isolated from shark cartilage (Sigma–Aldrich Chemical Co., St Louis, MO), phosphoric acid (H_3PO_4; EMD Chemicals Inc., Gibbstown, NJ), calcium nitrate ($Ca(NO_3)_2 \cdot 4H_2O$) and calcium hydroxide ($Ca(OH)_2$; Sigma–Aldrich Chemical Co., St Louis, MO). MCG slurries with varying mineral content (50% and 75% by weight) and the same overall density (0.042 g ml^{-1}) were prepared using the triple co-precipitation method described elsewhere [9,12,14,16–18]. Briefly, the collagen was mixed with H_3PO_4 solution at 15,000 rpm at room temperature in an overhead blender (IKA Works Inc., Wilmington, NC) for 60 min. Glycosaminoglycan was added to the collagen–H_3PO_4 mix using a peristaltic pump (Manostat, New York, NY) and mixed for another 60 min at 15,000 rpm. Dry-mixed $Ca(NO_3)_2 \cdot 4H_2O$ and $Ca(OH)_2$ were added to the collagen–glycosaminoglycan–H_3PO_4 solution and mixed for additional 15 min at 15,000 rpm. The slurry was poured into polysulfone molds (McMaster Carr Supplies, Dayton NJ) with dimensions of 12 × 3 × 1 cm (x-, y- and z-axes, respectively), placed in a freeze-drier at room temperature and then freeze-dried as described elsewhere [1,28,29,31,32]. Briefly, the slurry was cooled down to −20 °C at a cooling rate of 0.33 °C min^{-1} and kept at that temperature for 4 h for the slurry to completely freeze. Heat transfer was primarily in the through-thickness or z-direction. The frozen slurry was then sublimated at 25 °C under vacuum for 36 h to obtain the dry scaffold. A schematic of the scaffold fabrication process is shown in Fig. 1.

Two techniques were used to cross-link the scaffolds: (1) dehydrothermal treatment (DHT) and (2) 1-ethyl-3-(3-dimethylaminopropyl) carbodimide treatment (EDAC). The parameters for the DHT treatment were guided by previous work on CG scaffolds [11,17,18,24,27]. Briefly, the freeze-dried scaffold was placed under vacuum (50 mTorr) at a temperature of 105 °C for 24 h. The EDAC process

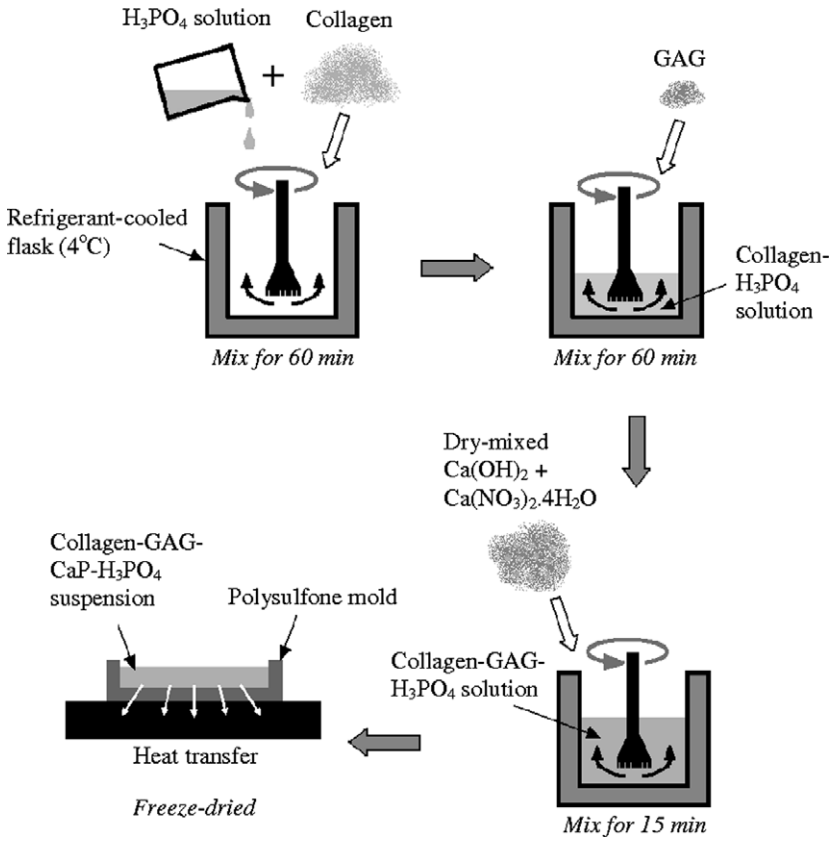

Fig. 1. Schematic of scaffold fabrication via triple co-precipitation method followed by freeze-drying.

was carried out on the scaffolds according to previously described methods [9,11,17,18]. A 5:2:1 ratio of EDAC:NHS:COOH (1-ethyl-3-(3-dimethylaminopropyl) carbodiimide:*N*-hydroxysuccinimide:carboxylic acid) was used for the current study. Briefly, the scaffolds were hydrated in deionized water for ~15 min; the required amount of EDAC/NHS solution was then mixed into the deionized water and the scaffold maintained in this solution for ~1 h. Samples were prepared and tested in the dry state as well as the hydrated state (soaked in 10% PBS solution for at least 12 h before testing). Six types of samples were prepared: (1) NX-DRY – non-cross-linked, dry scaffold; (2) DHT-DRY – dehydrothermal treatment, dry scaffold; (3) EDAC-DRY – EDAC cross-linked followed by drying via freeze-drying; (4) NX-HYD – non-cross-linked, hydrated; (5) DHT-HYD – dehydrothermal, hydrated; and (6) EDAC-HYD – EDAC cross-linked, hydrated.

2.2. Microstructural characterization

Relative density was calculated from the dry densities of collagen, brushite ($CaHPO_4 \cdot 2H_2O$) and monetite ($CaHPO_4$) according to:

$$\text{Relative density} = \rho^* \left(\frac{x_{\text{coll}}}{\rho_{\text{coll}}} + \frac{x_{\text{brushite}}}{\rho_{\text{brushite}}} + \frac{x_{\text{monetite}}}{\rho_{\text{monetite}}} \right) \quad (1)$$

where x_{coll}, x_{brushite} and x_{monetite} are, respectively, the weight fractions of collagen, brushite and monetite in the scaffold material (note that $x_{\text{coll}} + x_{\text{brushite}} + x_{\text{monetite}} = 1$), ρ_{coll}, ρ_{brushite} and ρ_{monetite} are, respectively, the densities of dry collagen, dry brushite and dry monetite and ρ^* is the density of the dry scaffolds. The weight fractions of brushite, monetite and collagen were determined using X-ray diffraction (XRD) as described below. The contribution of glycosaminoglycan was not considered, as the amount of glycosaminoglycan was much less than that of the other constituents. The mean pore diameter, D, on different planes (yz, xz and xy, where z is the through-thickness direction) was measured using the mean intercept method (D for a particular plane is the average of the major and minor axes of the best-fit ellipse on that plane) [29]; the ratio of the minor to the major axes of the best-fit ellipse gives the pore anisotropy ratio, R, on that plane [29]. Briefly, rectangular specimens randomly taken from five different locations of random dimensions were cut perpendicular to the three axes (corresponding to the three different planes as described above) and were embedded in glycomethacrylate (Polysciences Inc., Warrington, PA). The embedded specimens were cut into 5 μm thick sections at various depths using a Leica RM2165 microtome (Mannheim, Germany). The sectioned films were stained with aniline blue (Polysciences Inc., Warrington, PA) and observed under an inverted optical microscope (Nikon Optiphot, Japan) at 40× magnification. Images were obtained using a ccd color video camera (Optronics Engineering Inc., Goleta, GA) and image analysis was conducted

using Scion Image analysis software (Scion Corporation, Frederick, MD).

Semi-quantitative and qualitative analyses of the constituent mineral phases in the slurry as well as the dry scaffolds were carried out using XRD. Semi-quantitative analysis of the weight fractions of brushite and monetite was conducted using the reference-intensity-ratio method (with ~10% accuracy). Direct comparison between the highest peak intensity of the mix phase and the highest peak intensity produced by the pure phases was used to predict the weight fraction of different phases [47,48]. The slurries were mounted inside a silicate glass tube of 0.5 mm diameter and 0.001 mm thickness and the dry scaffolds were mounted on an aluminum holder by manually compressing the scaffold materials. For the slurry analysis, a D8 Discover XRD machine (Bruker AXS, Madison, WI) was used. The X-ray intersected the slurry-filled tube in the horizontal plane and the tube was oscillated in the vertical direction in order to scan a large amount of the slurry. The dry scaffold specimens were analyzed using the X'Pert PRO MPD XRD machine (PANalytical, Natick, MA). An incidence angle range of 5–75° was used, with a step size of 0.0167° and a dwell time of 36.83 s step^{-1}. For all scans, Cu Kα radiation was used, and XRD peak analysis was conducted using MDI Jade 7 software (Materials Data Inc, Livermore, CA).

Scanning electron microscopy (SEM; Leo VP438 SEM Leo Electron Microscopy Inc., Thornwood, NY) was used to study the pore structure of the scaffolds. Cylindrical specimens of 5 mm diameter were cut at random locations in the scaffolds using biopsy punches (Miltex Inc., York, PA). Specimens were mounted on an aluminum holder; the specimens were not gold coated. To study the mineral distribution through the wall thickness, specimens were embedded in resin (similar to the specimen preparation for pore size measurement, as described above) and 5 μm thick sections were sliced out. The backscattered electron detector was used under variable pressure mode to obtain the images. Elemental analysis was carried out using energy dispersive X-ray analysis (EDAX) in order to identify the calcium and phosphorous distributions.

Microtomography (Scanco USA Inc., Southeastern, PA) was used to analyze the three-dimensional calcium phase distribution in the scaffolds. Cubic specimens of $1 \times 1 \times 1$ cm were cut from the scaffolds perpendicular to the three axes and placed inside a glass tube. Cross-sectional images (with a resolution of 1024×1024 pixels) were acquired at different depths (seven images at intervals of 125 μm along the axis) for each of the specimens.

2.3. Mechanical properties of the scaffolds

Compressive stress–strain curves for the scaffolds were measured using a Zwick/Roell Z2.5 static materials tester (Zwick GmbH, Ulm, Germany). Cylindrical specimens, 5 mm in diameter and 3–6 mm thick, were cut at random locations in the scaffold along the three axes using biopsy punches (Miltex Inc., York, PA). All of the specimens were compressed at a uniform strain rate of 0.001 s^{-1} up to a maximum strain of 0.75. Poisson's ratio, v, of the dry scaffolds was measured by capturing images of the compressed specimen within the linear elastic regime of the stress–strain response. Images were acquired at a time interval of 0.2 s using a high-speed ccd camera (Retiga 1300; QImaging Corp., Canada) with a 200 mm lens (Nikon, Japan). Poisson's ratio (the negative ratio of lateral/applied strain) was measured from the images using the software analysis package, Vic 2D (Correlated Solutions, West Columbia, SC).

The Young's modulus of the solid comprising the scaffold, E_S, was measured via bending of individual, mineralized scaffold struts using an atomic force microscope (3DMFP; Asylum Research, Santa Barbara, CA). This is an established method of measuring the Young's modulus of microscale and nanoscale fibers [49–51]. E_S was measured for both the 50% and 75% by weight NX MCG scaffolds. Rectangular beams were cut from the pore walls of the scaffold using microsurgical forceps and a scalpel under an inverted optical microscope. As measured via optical microscopy (Nikon Optiphot, Japan), the length of the beams, L_{max}, varied from 40 to 120 μm; the width, b, varied from 25 to 90 μm; and the depth, h, varied from 3 to 12 μm. One end of each beam was bonded to a rigid support with cyanoacrylate, creating a cantilevered beam of length L from the support point (schematic shown in Fig. 2). The bending test was carried out using an AC160TS cantilever (Olympus, Tokyo, Japan) of stiffness 48.42 N m^{-1}, as measured via thermal power spectral density [49]. The force–deflection relation (F–Δ) of the beam is given by

$$\frac{F}{\Delta} = \frac{3E_S I}{L^3} \tag{2}$$

where the moment of inertia, $I = bh^3/12$. L could not be measured accurately from optical images of the beam set-up because the support point was not well-defined, but it was estimated by loading the cantilever at various points along the length of each strut (five to seven points) and measuring F vs. Δ for each loading point. The length between the loading point and the support point, L, was represented as $(L' + \lambda)$ where L' is the measured distance between the loading point and a reference point on the

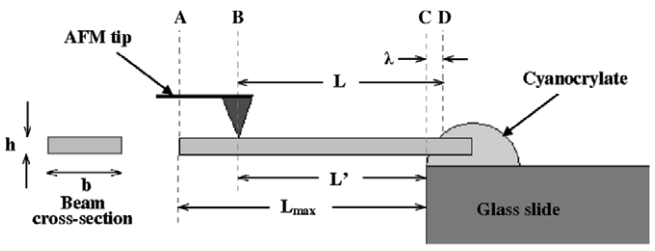

Fig. 2. Schematic of the experimental setup for the AFM bending test to determine modulus of the pore walls, E_S. Point A is the free end of the beam, point B is the loading point on the beam, point C is the reference point on the glass slide and point D is the support point of the beam.

support (the edge of the glass slide, as shown in Fig. 2) and λ is the distance between the support point and the reference point (note that λ is an unknown quantity). A typical F–Δ response is shown in Fig. 3a. A schematic diagram of the bending experiment is shown in the top-right of the figure. For each plot, F/Δ was measured from the slope of the initial retraction curve (as shown in Fig. 3a) to isolate the elastic response [49,50]. A graph of L' vs. $(\Delta/F)^{1/3}$ for the tests with the loading point at different points along the length of the beam was constructed (Fig. 3b). A straight line was fitted to these points with $R^2 > 0.95$ indicated that the beams were of uniform moment of inertia I ($I = bh^3/12$). The slope of this line is $(3E_SI)^{1/3}$ and the intercept is $-\lambda$ (see Eq. (2)). As I is known, E_S can be calculated. Five strut sections from each of the 50% and 75% by weight MCG scaffolds were tested in this manner.

The rupture strength of the solid, σ_{fS}, was estimated via nanoindentation using a Hysitron triboindenter (Hysitron Inc., Minneapolis, MN) [52–54]. Samples were cut from the walls of the mineralized scaffold pores using microsurgical forceps and a scalpel under an inverted optical microscope. The samples were bonded to a glass slide using cyanoacrylate and indented using a Berkovich indenter (Hysitron Inc., Minneapolis, MN). The load function consisted of three steps: (1) loading up to a nominal load of 75 μN at a rate of 7.5 μN s^{-1}; (2) saturating at 75 μN for 5 s; and (3) unloading to zero load at a rate of 7.5 μN s^{-1}. Twenty-five indents were conducted per sample and at least four samples were tested for each of the 50% and 75% by weight NX MCG scaffolds. A typical load–displacement curve for a 50% by weight MCG scffold in the NX-DRY state is shown in Fig. 4 (those for the 75% by weight MCG scaffold were similar). Rupture strength, σ_{fS}, was approximated from the calculated hardness, H, or mean pressure at maximum load as:

$$\sigma_{fS} \sim \sigma_{ys} = \frac{H}{3} = \frac{P_{max}}{3A_c} \tag{3}$$

where σ_{ys} is yield strength, P_{max} is the maximum indentation load and A_c is the projected area of contact. Note that this assumption of equivalence between the compressive yield strength and rupture strength of the mineralized pore wall material will tend to underestimate the actual rupture strength of the material, as the rupture strength will exceed the yield strength if the mineralized pore wall material effectively strain hardens upon yielding. Thus, the approximation in Eq. (3) should be considered a lower limit of the solid material rupture strength. Fused silica was used to calculate the machine compliance and the projected area of contact as a function of the contact depth. From the same load–displacement response, the elastic modulus of the sample, $E_S^{NX\text{-}DRY}$ was estimated from A_c and the slope

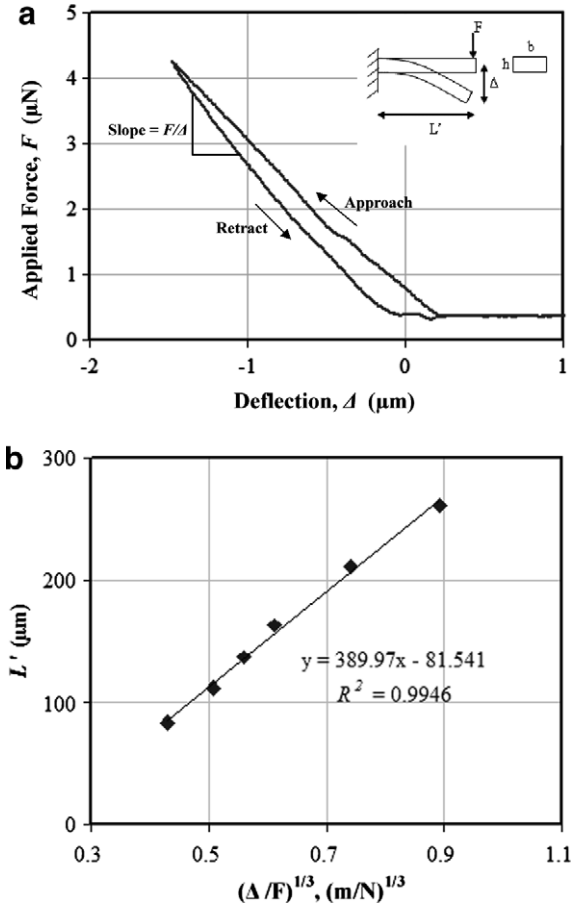

Fig. 3. (a) A sample bending force–deflection plot for a single beam of the 50% by weight MCG scaffold is shown. Similar plots were obtained for loading at different points along the length of the strut, L_{max}. From the L' vs. $(\Delta/F)^{1/3}$ plot, the modulus of the strut (E_S) was calculated (Eq. (2)). (b) Plot of L' vs. $(\Delta/F)^{1/3}$ for a 50% MCG beam is shown. Slope of this line fit is equal to $(3E_SI)^{1/3}$. Knowing the dimensions of the beam ($I = bh^3/12$), E_S can be calculated.

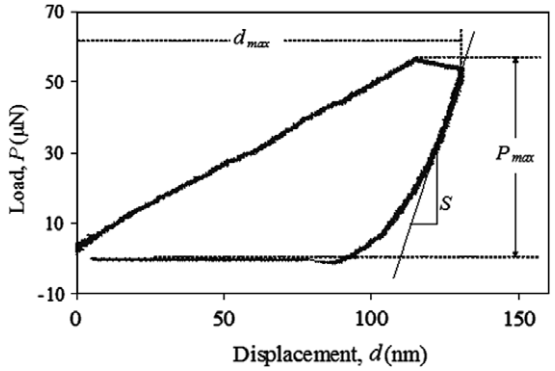

Fig. 4. A sample load–displacement plot for the 50% by weight MCG scaffold wall is shown. Similar plots were obtained for the 75% by weight MCG scaffold. Note that these nanoindentation experiments were conducted in open-loop load control, resulting in partial dissipation of the requested applied load via the transducer of this indenter. Thus, the maximum load exerted on the scaffold pore wall solid material was less than the requested magnitude of 75 μN. The dwell period at maximum load exhibits a slight decrease in load due to this open-loop feedback, as well as creep, but is not indicative of rupture or fracture of the mineralized pore wall. For this indenter geometry, indentation depths of 100 nm sample a contact area exceeding 0.2 μm^2 and a subsurface volume exceeding 0.04 μm^3, sufficient for at least some indentations to sample both the mineral and the polymer phases of the pore wall.

of the initial portion of the unloading curve, S (Fig. 4), according to the method of Oliver and Pharr [54].

2.4. Cellular solids model of the MCG scaffolds

The mechanical properties of cellular solids depend on relative density, the properties of the solid of which the cellular solid is made (such as density, ρ_S, Young's modulus, E_S, and rupture strength, σ_{fS}) and the cell geometry (e.g. open or closed cells) [4,27,30]. Simple relationships between overall foam properties (such as Young's modulus, E^*, and strength, σ^*) and the relative density and solid cell wall properties can be derived using dimensional analysis [4,30]. Key relationships for open-cell foams that are relevant for mechanical characterization of the scaffolds are given below:

$$\frac{E^*}{E_S} = \left(\frac{\rho^*}{\rho_S}\right)^2 \tag{4}$$

$$\frac{\sigma^*}{\sigma_{fS}} = 0.2\left(\frac{\rho^*}{\rho_S}\right)^{\frac{3}{2}} \tag{5}$$

2.5. Statistical analysis

One-way analysis of variance (ANOVA) and Fisher's protected least significant difference (Fisher's PLSD) methods were used to determine statistical significance between different sets of data and pair-wise data sets, respectively. A probability value of 95% ($P < 0.05$) was used to determine the significance. All the measurements are reported as mean ± standard deviation. The symbols *, ** and *** indicate statistically significantly different results.

3. Results

3.1. Microstructural characterization

The experimentally measured overall scaffold densities (ρ^*) for the 50% and 75% by weight MCG scaffolds were 0.063 ± 0.0015 and 0.06 ± 0.0034 g cm^{-3}, respectively. The densities are statistically significantly different ($P = 0.039$), even though the target slurry densities were the same (0.042 g ml^{-1}). The difference arises from the fact that some of the calcium phosphate phase adhered to the surface of the beaker while mixing. The relative densities can be calculated using Eq. (1). For the 50% scaffold, $x_{coll} = 0.5$, $x_{brushite} = 0.485$ and $x_{monetite} = 0.015$, while for the 75% scaffold, $x_{coll} = 0.25$, $x_{brushite} = 0.503$ and $x_{monetite} = 0.248$; these results are described in further detail below. The densities for dry collagen, brushite and monetite are 1.3, 2.33 and 2.93 g cm^{-3}, respectively [24,55–57]. Relative densities for 50% and 75% by weight MCG scaffolds are calculated to be 0.038 ± 0.001 and 0.030 ± 0.002, respectively. The 75% scaffold was observed via SEM to have a bilayer structure with small pores in the top layer, closer to the air side during freeze-drying, and larger pores in the bottom layer, closer to the cooling plate on the base. The densities of these layers were measured separately by sectioning the scaffold at the interface and punching out specimens from both the layers. The relative densities were 0.032 ± 0.003 and 0.024 ± 0.002 for the top and bottom layers, respectively. The characteristics of the bilayer are described in more detail below.

Optical images of an embedded specimen perpendicular and parallel to the z-axis, through the thickness of the scaffold sheet, are shown in Fig. 5. The 50% by weight MCG scaffold exhibited a uniform microstructure throughout the scaffold, with a roughly uniform pore size and interconnected walls throughout. The 75% by weight MCG scaffold exhibited a bimodal pore size distribution, with smaller pores and interconnected walls in the top zone and larger pores and disconnected walls in the bottom zone. The mean pore diameter, D, and anisotropy ratios, R, on the three different planes are listed in Table 1; for the 75% scaffold, measurements for the top and bottom layers are reported separately. R on different planes were >0.92 and D on different planes were similar; the pores are roughly equiaxed for both scaffolds. The average pore diameter was calculated by averaging all the values (on different planes). The average pore diameter for the 50% scaffold was 202 ± 25 μm. The average pore diameters of the 75% scaffold for the top and bottom parts of the scaffold were 227 ± 31 and 343 ± 38 μm, respectively. These values were statistically significantly different ($P < 0.05$).

Fig. 6a shows the XRD plots for the 50% and 75% by weight MCG slurries. The straight lines represent brushite peaks. It is apparent that both slurries exhibited 100% brushite as the only mineral phase. Fig. 6b shows the XRD plots for the NX-DRY MCG scaffolds. Based on the reference intensity ratio method as described above, the 50% scaffold comprised 97 wt.% brushite and 3 wt.% monetite as the crystalline phases, while the 75% scaffold comprised 67 wt.% brushite and 33 wt.% monetite as the crystalline phases.

SEM micrographs of the 50% and 75% by weight MCG scaffolds (images taken of the plane perpendicular to the z-axis) are shown in Fig. 7. The scaffolds exhibit a homogeneous distribution of mixed open- and closed-cell microstructure with interconnected pores (Fig. 7a and b). Unlike unmineralized CG scaffolds [27,29,31], MCG scaffolds exhibited pore walls as well as thin struts. EDAX analysis showed that the white particles through the thickness of these walls (Fig. 7c and d) were calcium- and phosphorous-rich particles. As described above, XRD results confirmed these particles to be either brushite or monetite. The more highly mineralized scaffold had a denser packing of calcium phosphate. The denser calcium phosphate packing in the 75% by weight MCG scaffold caused a large variation in the wall thickness (Fig. 7c and d). Microtomographic images confirmed that the mineral phases were distributed homogeneously throughout the walls and struts of the scaffolds. Mineral phase particle size ranged from 100s nm to μm with a mode cross-sectional area of

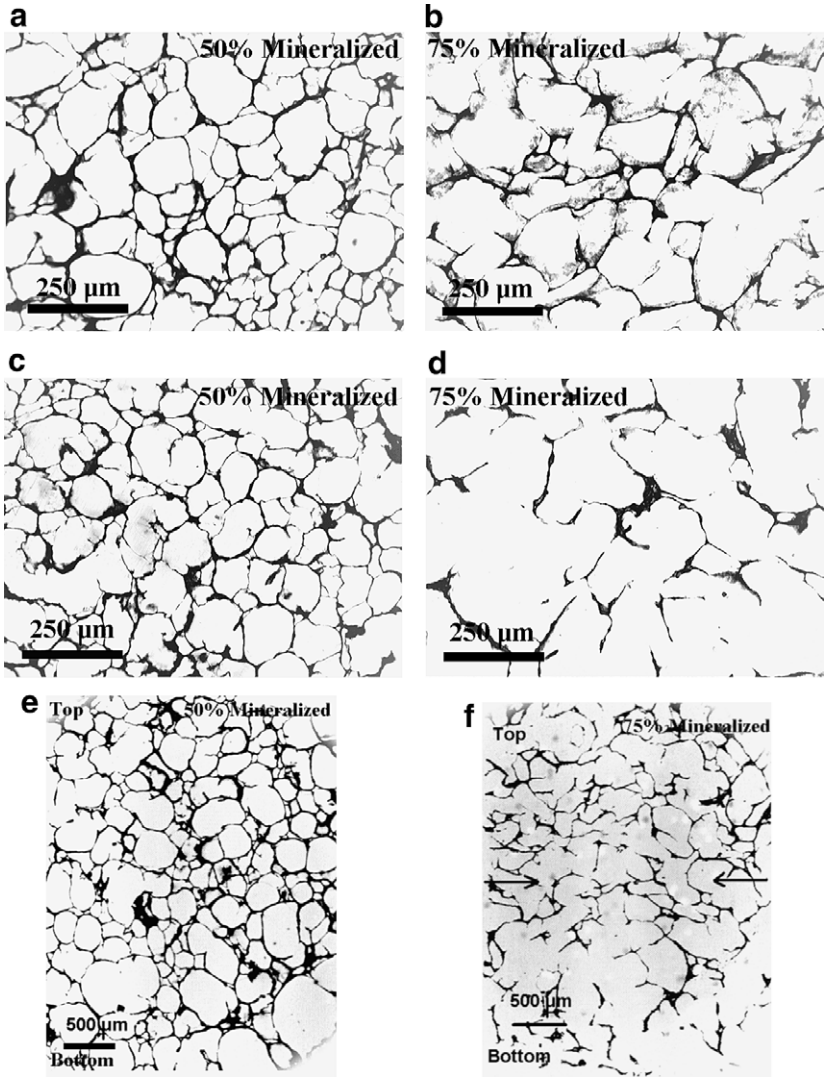

Fig. 5. Optical micrographs of embedded MCG scaffolds with planes perpendicular to the *z*-axis: (a, c) 50% by weight scaffold and (b, d) 75% by weight scaffold, taken at different depths along the *z*-axis. (e, f) Entire cross-section of plane parallel to the *z*-axis for the 50% and 75% by weight MCG scaffolds, respectively, showing uniform pore size distribution for the 50% scaffold and bimodal pore size distribution for the 75% scaffold.

Table 1
Pore size measurements for the 50% and 75% by weight NX-DRY MCG scaffolds

Scaffold	Plane	*D* (μm)	*R*
50% NX	*yz*	$216 \pm 26.0^{*}$	0.972 ± 0.023
	xz	194 ± 21.0	0.966 ± 0.039
	xy	196 ± 23.1	0.957 ± 0.035
75% NX	*yz*-Top	214 ± 26.8	0.955 ± 0.040
	xz-Top	242 ± 17.6	0.939 ± 0.049
	xy-Top	224 ± 42.6	0.922 ± 0.075
	yz-Bottom	344 ± 42.0	0.929 ± 0.053
	xz-Bottom	342 ± 42.2	0.959 ± 0.049
	xy-Bottom	343 ± 31.9	0.963 ± 0.042

* Indicates that statistically different value.

$\sim$1.3 μm^2 (calculated from Fig. 7). The 50% scaffold has a uniform pore size throughout the entire scaffold. However, both SEM and microtomographic images of the 75% scaffold indicated a distinct boundary between the top portion of the scaffold, which had smaller pores, and the bottom portion of the scaffold, which had larger pores (Fig. 8). The boundary between the two zones varied from near the edge of the sample to the center of the sample. SEM and optical micrographs indicated defects such as voids and cracks in the walls and struts of the MCG scaffolds (Fig. 9a and b), as well as disconnected pore walls and struts (Fig. 9c and d). The 75% by weight MCG scaffold exhibited more defect sites than the 50% scaffold.

3.2. Mechanical characterization

A typical compressive stress–strain curve for a 50% by weight MCG scaffold in the dry state is shown in Fig. 10 (those for the 75% by weight MCG scaffold were similar). Distinct linear elastic, collapse plateau and densification regimes were observed. Elastic modulus (E^{*}), collapse strength and strain (σ^{*} and ε^{*}, respectively) and collapse

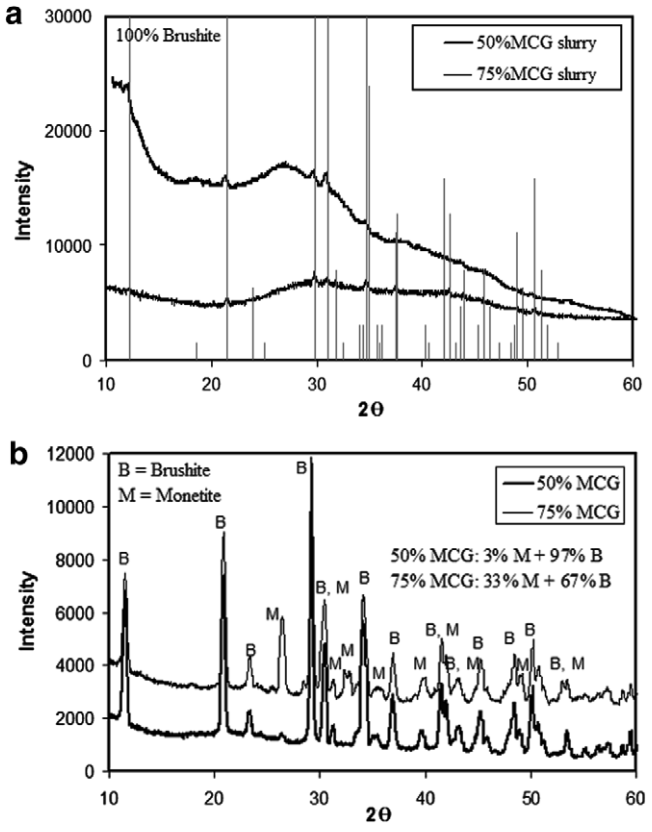

Fig. 6. (a) X-ray diffraction plots for the 50% and 75% by weight MCG slurries are compared in this figure. The vertical lines represent brushite peaks. (b) X-ray diffraction plots for the dry 50% and 75% by weight MCG scaffolds are compared in this figure. The 50% scaffold has mostly brushite, while the 75% scaffold has a significant amount of monetite along with brushite.

modulus ($\Delta\sigma/\Delta\varepsilon$) were measured from the stress–strain curve. E^* is the slope of the linear elastic regime, $\Delta\sigma/\Delta\varepsilon$ is the slope of the collapse regime, σ^* and ε^* are the point of transition from linear to the collapse regime (determined from the intersection of the E^* and $\Delta\sigma/\Delta\varepsilon$ regression lines). Curves of similar shape, but lower modulus and strength, were obtained for the hydrated states of the scaffolds.

The values of E^*, σ^*, ε^* and $\Delta\sigma/\Delta\varepsilon$ for loading along the three axes for the 50% and 75% by weight MCG scaffolds in the NX-DRY state are listed in Table 2. The Young's moduli of the 50% scaffold are typically about twice those of the 75% scaffold and the strengths of the 50% scaffold are typically about three times those of the 75% scaffold. The 75% scaffold has a lower E^* and σ^* in the z-direction, due in part to the two layers of different densities through the height of the scaffold. For both scaffolds, ε^* is of the order of 10–15%. Collapse moduli of the 50% scaffold are higher than those of the 75% scaffold.

The values of E^*, σ^*, ε^* and $\Delta\sigma/\Delta\varepsilon$ in the z-direction for scaffolds with the different cross-linking treatments are listed in Table 2. The properties for the hydrated 75% by weight MCG scaffold could not be determined, as the slope difference between the linear elastic regime and the collapse plateau regime was negligible. The specific cross-linking treatments had no statistically significant effect on any of the properties ($P > 0.05$) for both scaffolds in the dry state, with the exception of the DHT treatment on the 75% mineralized scaffold. As expected, the hydrated state exhibits a much lower E^*, σ^* and $\Delta\sigma/\Delta\varepsilon$ than that of the dry state for the 50% scaffolds. In the hydrated state, DHT and EDAC cross-linking increase the E^*, σ^* and $\Delta\sigma/\Delta\varepsilon$ over that of the non-cross-linked scaffold by 1.5 and 5 times, respectively. There was no statistically significant effect on the collapse strain, ε^*, with the exception of the EDAC cross-linking.

For the 75% by weight NX-DRY MCG scaffold, the Young's modulus and collapse strength in the z-direction of the top and bottom zones, which are of different pore sizes and densities, were measured separately. The scaffold was cross-sectioned perpendicular to the z-axis at the boundary between the zones (determined by visual inspection) to obtain two separate pieces with the two different pore sizes. Fig. 11 shows E^* and σ^* for the top and the bottom zones of the 75% NX MCG scaffold, along with the overall E^* and σ^*. As expected from a simple lower-bound composites model, the overall E^* lies between that of the top and bottom layers.

The Poisson's ratios for the 50% and 75% by weight NX-DRY MCG scaffolds were measured to be 0.02 ± 0.005 and 0.02 ± 0.007, respectively (samples were loaded in the z-direction). These are negligible compared to the expected value of ν for open-cell foam (i.e. 0.3) [4].

Young's moduli of the solid, $E_S^{\text{NX-DRY}}$, for the 50% and 75% by weight NX-DRY MCG scaffolds were measured to be 9.15 ± 0.983 and 6.31 ± 1.43 GPa, respectively (based on the AFM bending test). $E_S^{\text{NX-DRY}}$ varied from ~7.8 to 10.5 GPa and from 4.5 to 7.7 GPa for the 50% and 75% by weight scaffolds, respectively. These results can be linearly extrapolated to the cross-linked and hydrated states, based on the relative difference in E^* for different states (e.g. $E_S^{\text{DHT-DRY}} = E_S^{\text{NX-DRY}} \times \left[E^*_{\text{DHT-DRY}}/E^*_{\text{NX-DRY}}\right]$ and $E_S^{\text{DHT-HYD}} = E_S^{\text{DHT-DRY}} \times \left[E^*_{\text{DHT-HYD}}/E^*_{\text{DHT-DRY}}\right]$ [27].

Measurement of rupture strength of the solid, σ_{fS}, based on nanoindentation, is an approximation to the actual strength of the composite, as the variation in σ_{fS} was much larger than that of E_S (measured through the AFM beam-bending experiment), depending on the local composition of the point of indentation. As seen in Fig. 7c and d, the pore walls consisted of CG matrix reinforced with mineral phases. Since the area indented was nanoscale in volume (see Fig. 4), the extreme values plausibly corresponded to the mechanical response of the CG matrix phase and the mineral phases. σ_{fS} varied from ~0.5 to 300 MPa and from 30 to 350 MPa for the 50% and 75% by weight NX-DRY MCG scaffolds, respectively. However, for calculations of scaffold mechanical properties based on the cellular solids model, the values of σ_{fS} within this range were chosen from the subset of nanoindentation experiments that predicted the same E_S as that obtained from AFM beam-bending tests. Both the beam-bending experiments and pore-wall-indentation experiments probed the Young's modulus of

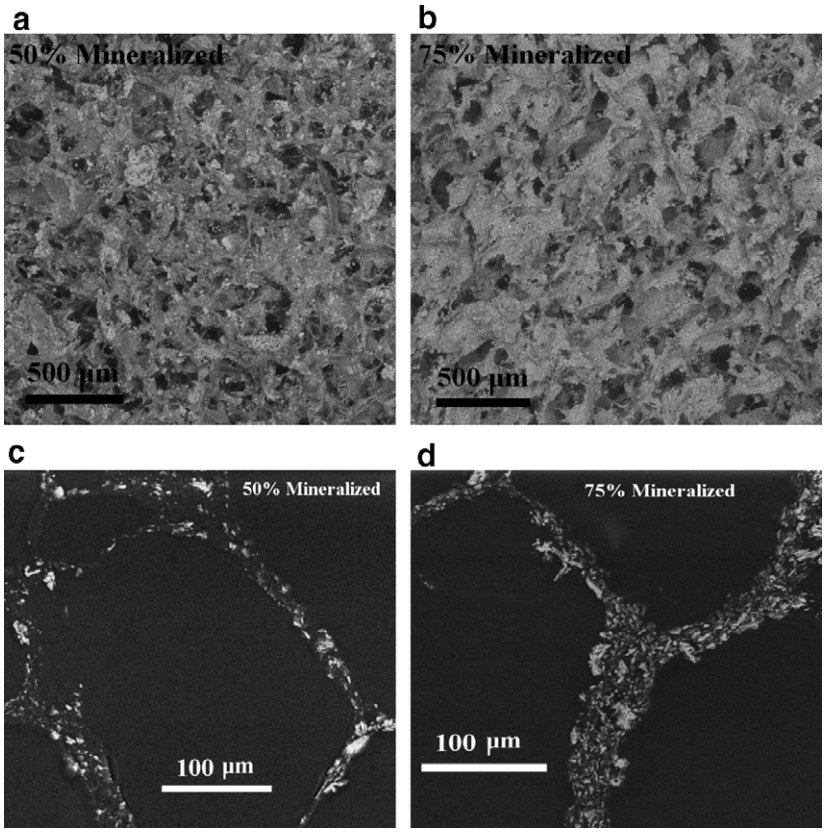

Fig. 7. (a, b) SEM images for the 50% and 75% by weight MCG scaffolds measured on the 5 mm diameter punched out of the scaffolds. (c, d) Mineral distribution through the thickness of the pore walls measured on the 5 μm thick resin-embedded samples.

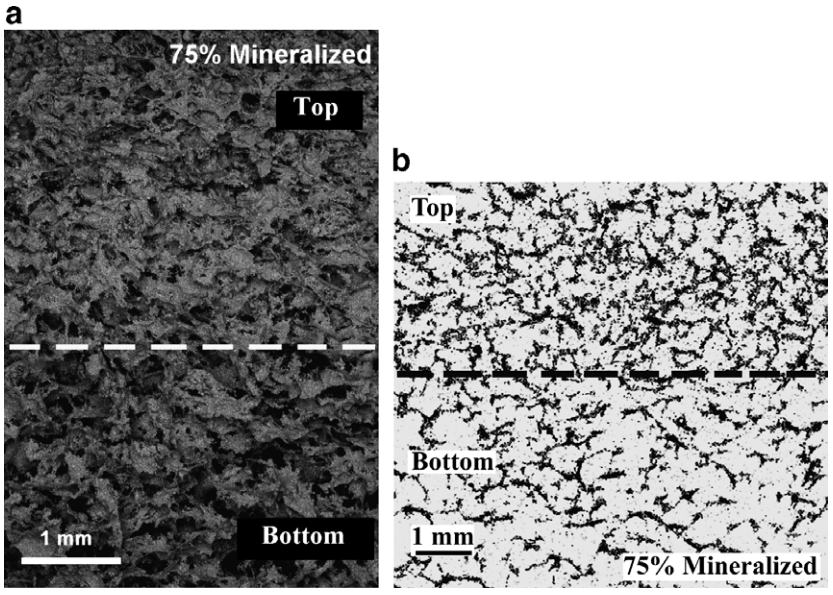

Fig. 8. Bimodal pore size distribution in the 75% by weight MCG scaffold is demonstrated in (a) the SEM and (b) the micro-CT images. The arrows separate the section with smaller pores (top) from that with larger pores (bottom).

the solid, E_S; the former approach captures the modulus over a larger volume than is represented by the nanoindented volumes. Thus, we assume that the mineralized composite (volume-averaged) mechanical response is best represented by nanoindented regions of the mineralized pore wall that exhibited the same modulus as that measured via beam-bending. This assumption is supported by the fact that the mode mineral phase cross-sectional area of 1.3 μm^2 exceeds the projected area of contact of these indentations computed from probe geometry and

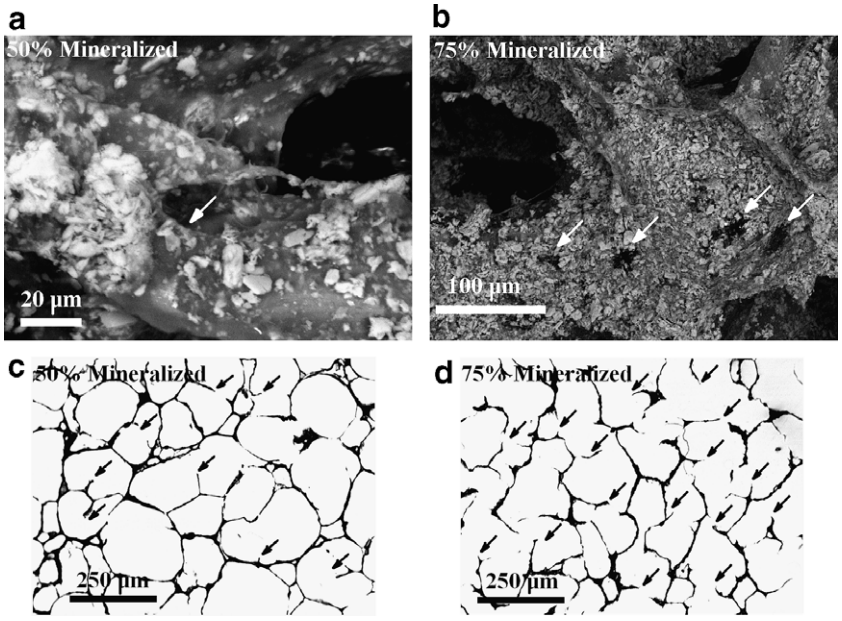

Fig. 9. (a, b) SEM images of the 50% and 75% by weight MCG scaffolds showing voids on the pore walls. (c, d) Optical images of the 50% and 75% by weight MCG scaffolds showing disconnected walls and struts.

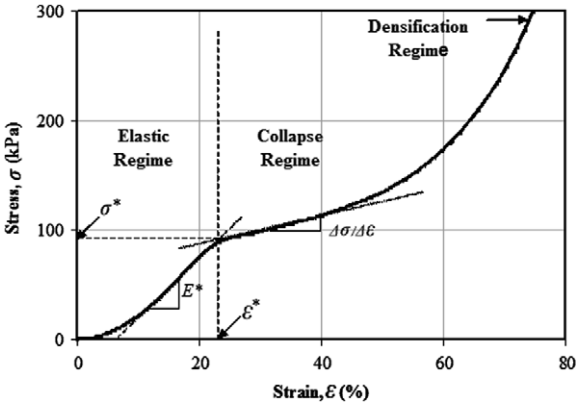

Fig. 10. A typical compressive stress–strain curve for a 50% by weight NX-DRY MCG scaffold. The slope in the linear elastic regime is the modulus of the scaffold (E^*), the slope in the collapse regime is the collapse modulus ($\Delta\sigma/\Delta\varepsilon$) and the point of intersection of the regression lines for modulus and collapse modulus are characterized by collapse strength (σ^*) and collapse strain (ε^*). The 75% by weight MCG scaffold had a similar stress–strain curve.

maximum depth (0.24 μm^2). Given the wide mineral phase particle size distribution (Fig. 7), an array of indentations of this size could sample the stiff particles, the compliant CG pore wall and a composite mixture of these two phases. The solid wall modulus, E_S, measured from the nanoindentation tests, varied from ~19 MPa to 13.4 GPa and from 2 to 25 GPa for the 50% and 75% by weight NX-DRY MCG scaffolds, respectively. As noted above, the range of E_S obtained from the AFM bending test was within the range obtained from the nanoindentation tests. The resulting strengths of the solid materials making up the scaffold struts, σ_{fS}, were 201 ± 52 MPa and 149 ± 66 MPa for the 50% and 75% by weight MCG NX-DRY scaffolds, respectively. These results can be linearly extrapolated to the cross-linked and hydrated states, based on the relative difference in σ^* for different states (similar to Young's modulus predictions for different states, as described above).

4. Discussion

The pore sizes for both scaffolds were in the range of 200–350 μm, which is optimal for bone growth [26,58–60]. For both scaffolds, the mineral phase was distributed throughout the walls, which is an improvement over existing mineralized scaffolds in which the mineral simply coats the outside of the collagen struts [39–43].

There were substantial differences in the microstructure and mechanical properties of the 50% and 75% by weight MCG scaffolds. The 50% scaffold had a higher relative density, as well as a more uniform density and pore size than the 75% scaffold. The walls of the 75% scaffold were more variable in thickness along their length and were less well connected, with ruptures and cracked walls visible in the SEM images, compared with the 50% scaffold.

Bone mineral closely resembles hydroxyapatite, a calcium phosphate. Scaffolds for bone regeneration usually involve some form of calcium phosphate, typically hydroxyapatite [33,61] or tricalcium phosphate [43,62]. In our scaffolds, most of the calcium phosphate exists as brushite, which can be converted to octacalcium phosphate and then to apatite by hydrolysis. Monetite, on the other hand, does not convert to octacalcium phosphate [9,11,63,64]. The 50% scaffold was comprised chiefly of brushite (97 wt.%), while the 75% scaffold was comprised of 66 wt.% brushite and 33 wt.% monetite. In the 75% MCG scaffold, some of the brushite in the slurry phase transformed to monetite during freeze-drying (note that

Table 2
Mechanical properties of the 50% and 75% by weight MCG scaffolds determined from the compression tests

Scaffold	Axis	E^* (kPa)	σ^* (kPa)	ε^* (%)	$\Delta\sigma/\Delta\varepsilon$ (kPa)
Effect of loading direction (dry)					
50% NX-DRY	x	$1000 \pm 267^*$	$102 \pm 9.03^*$	10.4 ± 2.29	103 ± 41.6
	y	615 ± 146	88 ± 8.69	13.9 ± 3.38	111 ± 35.9
	z	720 ± 215	83 ± 11.2	12.4 ± 3.82	123 ± 37.4
75% NX-DRY	x	403 ± 152	33.8 ± 5.79	9.01 ± 2.78	77.2 ± 20.3
	y	495 ± 119	$43.1 \pm 9.99^*$	8.87 ± 1.41	67.4 ± 19.3
	z	$204 \pm 36.8^*$	28.4 ± 4.81	$13.4 \pm 1.06^*$	$112 \pm 15.4^*$
Scaffold	Cross-link	E^* (kPa)	σ^* (kPa)	ε^* (%)	$\Delta\sigma/\Delta\varepsilon$ (kPa)
Effect of different cross-linking treatments (dry): tested in the z-direction					
50%	NX-DRY	720 ± 215	83 ± 11.2	12.4 ± 3.82	123 ± 37.4
	DHT-DRY	853 ± 99.0	97.5 ± 11.6	11.4 ± 0.72	158 ± 34.8
	EDAC-DRY	759 ± 230	88.0 ± 14.6	12.5 ± 3.99	139 ± 45.7
75%	NX-DRY	204 ± 36.8	28.4 ± 4.81	13.4 ± 1.06	112 ± 15.4
	DHT-DRY	274 ± 51.6	$48.3 \pm 18.0^*$	$17.1 \pm 3.81^*$	160 ± 48.6
	EDAC-DRY	230 ± 110	29.8 ± 12.0	13.6 ± 2.84	87.5 ± 73.5
Scaffold	Cross-link	E^* (kPa)	σ^* (kPa)	ε^* (%)	$\Delta\sigma/\Delta\varepsilon$ (kPa)
Effect of different cross-linking treatments (hydrated): tested in the z-direction					
50%	NX-HYD	$3.86 \pm 0.738^*$	0.341 ± 0.060	9.78 ± 1.90	$1.95 \pm 0.187^*$
	DHT-HYD	$6.20 \pm 1.51^{**}$	0.547 ± 0.089	9.60 ± 3.02	$3.05 \pm 0.392^{**}$
	EDAC-HYD	$15.2 \pm 1.68^{***}$	$2.08 \pm 0.337^*$	$13.3 \pm 3.26^*$	$8.54 \pm 1.25^{***}$
75%	The properties of the scaffolds could not be determined as the slope difference between the linear elastic regime and the collapse plateau regime was negligible. The behavior could not be idealized as that of open-cell foams				

Note: results are reported as mean ± standard deviation; *, **, and *** denote distinct, statistically significant results via ANOVA.

monetite is a dehydrated form of brushite). During this phase change, the by-product (i.e. water) was liberated to the immediate vicinity of the scaffold walls and struts, making this scaffold partially hydrated even after extended sublimation. This was evident from the adhesive nature of the scaffold upon handling. The phase concentration is believed to be due to the higher concentration of H_3PO_4 used in the synthesis of the 75% by weight scaffold. During sublimation, with a decrease in pressure, water vaporizes faster than H_3PO_4 (the vapor pressure of H_3PO_4 is much lower than that of water at 25 °C), increasing the pH of the residual solvent. Monetite is a more stable phase than brushite at lower pH and therefore it is possible that the phase change is driven by the high residual concentrations of H_3PO_4 during sublimation. The 75% scaffold had a denser packing of mineral, as expected from the increased weight fraction of mineral.

The compressive stress–strain curves for the scaffolds exhibited shapes characteristic of cellular solids, with the three regimes corresponding to linear elasticity, cell collapse and, at high strains, densification [4]. The Young's modulus and compressive strength of the 50% scaffold were higher than those of the 75% scaffold. This was expected from the lower stiffness and strength of the 75% scaffold struts and the lower relative density of the 75% scaffold. The inferior strut properties of the highly mineralized scaffold are attributed to the water retention of the scaffold, as described above. The Young's modulus and strength of these scaffolds are in the lower range, relative to mineralized scaffolds made by other techniques (Table 3).

We can compare the measured properties of the scaffolds with values predicted from engineering models. We first estimate the modulus of the solid strut material, using a simple Voigt–Reuss composite model, and then estimate the modulus of the scaffold, using a cellular solids model [4]. The upper and lower bounds on the Young's modulus of the solid for the 50% by weight MCG scaffolds are estimated from the composites model, based on the Young's modulus of collagen and brushite. The Young's modulus of collagen struts in a DHT-DRY CG scaffold has been measured to be 762 ± 35.4 MPa, from AFM-enabled strut bending tests [27]. The Young's modulus of brushite is assumed to be similar to that of hydroxyapatite (~110 GPa) [19,65]. The volume fractions of collagen and brushite in the 50% by weight MCG scaffold are 0.642 and 0.358, respectively (based on the mass fractions obtained from the XRD results, as described above). The composite Young's modulus of the solid for the 50% DHT-DRY scaffold is predicted to range between 1 and 40 GPa. Our measured value of the solid strut modulus $E_S^{\text{NX-DRY}}$ for the 50% scaffold is 9.15 GPa, while that estimated for the DHT-DRY scaffold, $E_S^{\text{DHT-DRY}}$, is 10.84 GPa; both values are closer to the lower bound of this composite model, as might be expected from the unaligned distribution of brushite within the struts. The Young's modulus of the dry MCG scaffold strut material is comparable to wet cortical bone (~10–20 GPa).

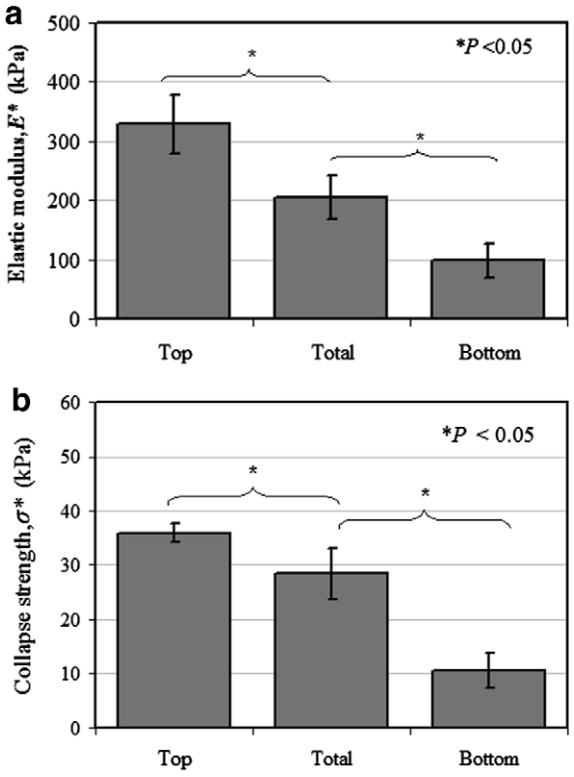

Fig. 11. (a, b) Young's modulus (E^*) and collapse strength (σ^*) of each of the layers of the 75% by weight NX-DRY MCG scaffolds of differing density and pore size, compared with the overall modulus and strength of the scaffold. All the modulus and strength values are measured along the z-direction ($E^*_{\text{Top}} = 329 \pm 48.9$ kPa, $E^*_{\text{Bottom}} = 98.2 \pm 28.5$ kPa and $E^*_{\text{Total}} = 204 \pm 36.8$ kPa; $E^*_{\text{Top}} = 36 \pm 1.73$ kPa, $E^*_{\text{Bottom}} = 10.7 \pm 3.21$ kPa, $E^*_{\text{Total}} = 28.4 \pm 4.81$ kPa).

Cellular solids models for open-cell foams predict values of Young's modulus, E_S, and compressive strength, σ_{fS}, of the 50% DHT-DRY scaffold of 15.7 and 0.35 MPa (Eqs. (4) and (5)), respectively, compared with our experimentally observed values of $E^* = \sim 0.8$ MPa and $\sigma_{fS} = \sim 0.100$ MPa. For the 75% scaffold, the model predicts $E^* = 5$ MPa and $\sigma_{fS} = 0.14$ MPa, compared with our experimentally observed $E^* = \sim 0.4$ MPa and $\sigma_{fS} = \sim 0.04$ MPa. The modulus and strength data are factors of ~10–15 and 3 times lower than the values given by the cellular solids model, respectively. Possible reasons for the discrepancy include the observed presence of defects, such as voids and cracks in the walls and struts of the scaffold, as well as disconnected walls and struts [66–69]. This was apparent from the SEM and optical images of the scaffolds (Fig. 9). The above reduction in properties correspond to 25–40% defects by volume in the scaffold [67]. In addition, our approximation of the scaffold pore wall rupture strength (as measured via nanoindentation) tends to underestimate the actual strength of the scaffold solid, such that one would reasonably expect the cellular solids model prediction to underestimate the experimentally measured scaffold strength.

The mechanical properties of scaffolds in this study are lower than those of scaffolds described in the literature (Table 3). They are also substantially lower than theoretically predicted by engineering models, suggesting that they can be improved with appropriate control of the microstructure. In our future work, we seek to improve the mechanical properties of the scaffolds.

5. Conclusion

MCG scaffolds with 50% and 75% by weight mineral content were fabricated via a titrant-free triple co-precipitation method followed by freeze-drying. The pore sizes for both scaffolds were in the range of 200–350 μm, which is optimal for bone growth [26,58–60]. For both scaffolds, the mineral phase was distributed throughout the walls, which mimics bone and is an improvement over existing mineralized scaffolds in which the mineral simply coats the outside of the collagen struts [39–43]. The 50% NX-DRY scaffold had brushite as the major mineral phase with a negligible amount of monetite (~3 wt.%), while the 75% NX-DRY scaffold was comprised of ~67 wt.% of brushite and 33 wt.% of monetite. The elastic moduli and strength of the 50% scaffold were typically about twice and three times those of the 75% scaffold, respectively. This

Table 3
Elastic moduli, E^*, collapse strengths, σ^*, and porosities of various bone-regenerating composite scaffolds based on natural polymers and calcium phosphate ceramics

Scaffold	E^* (kPa)	σ^* (kPa)	Porosity (%)	Reference
Dry				
Mineralized CG (50% by weight mineral)	762	85	85	[11]
Mineralized CG (50% by weight mineral)	720–1000	83–102	96	Current scaffold
Mineralized CG (75% by weight mineral)	204–495	28–43	97	Current scaffold
Chitosan/tricalcium phosphate	1000–3000	100–300	90	[43]
Gelatin/hydroxyapatite (10–30% by weight mineral)	2280–4010	–	85	[33]
Chitosan/gelatin/tricalcium phosphate	830–10,880	90–880	–	[62]
Collagen/alginate/hydroxyapatite	50,000–350,000	5000–25,000	65–80	[61]
Hydrated				
Mineralized CG (50% by weight mineral)	4–15	0.34–2	96	Current scaffold
Collagen/hydroxyapatite (70% by weight mineral)	37–75	–	87–95	[70]
Collagen/hydroxyapatite (80% by weight mineral)	50–300	30–60	95	[71]

unexpected decrease in Young's modulus and strength with increasing mineral content was attributed to lower solid properties, lower relative density and more defect sites in the highly mineralized scaffold. The mechanical properties of the scaffolds in this study are lower than those of mineralized scaffolds made by other techniques, as well as cortical and cancellous bone. The mechanical properties of the scaffolds in this study are also less than the values predicted by engineering models, suggesting that there is potential for improved performance with appropriate control of the microstructure, to eliminate voids and unsupported walls and struts. Future research is directed towards modifying the current fabrication techniques to obtain mechanically stiffer and stronger scaffolds.

Conflicts of interest statement

Lorna J. Gibson has a financial interest in Orthomimetics, a start up firm that resulted from a previous collaboration on a similar mineralized collagen scaffold. However, the authors did not receive any financial support from Orthomimetics for this project.

Acknowledgements

Funding for this project was provided by the National Science Foundation, Grant No. CMS-0408259. The authors acknowledge Drs. Brendan Harley and Andrew Lynn for offering their assistance and valuable discussions. The authors are grateful to Professor David Cory and Dr. Chandrasekhar Ramanathan in the Department of Nuclear Science and Engineering, Professor Elazer Edelman and Philip Seifert in the Harvard–MIT Division of Health Sciences & Technology, Mr. Alan Schwartzman in the MIT Department of Materials Science and Engineering's Nanomechanical Technology Laboratory and Ms. Kristin Myers in the Department of Mechanical Engineering for the facilities and assistance that helped complete this research.

References

[1] Yannas IV, Spector M. Design of medical devices and implants, MIT Course No: 3.961, 2006.
[2] Harley BA, Cell-matrix interactions: collagen–GAG scaffold fabrication, characterization, and measurement of cell migratory and contractile behavior via confocal microscopy, MIT Thesis, 2006. p. 1–393.
[3] Ashman RB, Cowin SC, Van Buskirk WC, Rice JC. A continuous wave technique for the measurement of elastic properties of cortical bone. J Biomech 1984;17:349.
[4] Gibson LJ, Ashby MF. Cellular solids – structure and properties. 2nd edition. Cambridge: Press Syndicate of the University of Cambridge; 1997.
[5] Gross KA, Rodrýguez-Lorenzo LM. Biodegradable composite scaffolds with an interconnected spherical network for bone tissue engineering. Biomaterials 2004;25:4955–62.
[6] KellomaKi M, Niiranen H, Puumanen K, Ashammakhi N, Waris T, Tormala P. Bioabsorbable scaffolds for guided bone regeneration and generation. Biomaterials 2000;21:2495–505.
[7] Xiong Z, Yongnian Y, Shenguo W, Zhang R, Zhang C. Fabrication of porous scaffolds for bone tissue engineering via low-temperature deposition. Scripta Mater 2002;46:771–6.
[8] Yang CR, Wang YJ, Chen XF, Zhao NR. Biomimetic fabrication of BCP/COL/HCA scaffolds for bone tissue engineering. Mater Lett 2005;59:3635–40.
[9] Harley BA, Lynn AK, Wissner-Gross Z, Bonfield W, Yannas IV, Gibson LJ. Design of a multiphase osteochondral scaffold III: fabrication of a mineralized collagen–GAG scaffold, J Biomed Mater Res (Part A), submitted for publication.
[10] Lu HH, El-Amin SF, Scott KD, Laurencin CT. Three-dimensional, bioactive, biodegradable, polymer–bioactive glass composite scaffolds with improved mechanical properties support collagen synthesis and mineralization of human osteoblast-like cell in vitro. J Biomed Mater Res, Part A 2003;64A:465–74.
[11] Lynn AK, Cameron RE, Best SM, Brooks RA, Rushton N, Bonfield W. Design and development of an osteochondral scaffold. PhD Thesis (Department of Materials Science and Metallurgy), University of Cambridge, 2005. p. 1–165.
[12] Lynn AK. Phase mapping: a novel design approach for the production of calcium phosphate–collagen biocomposites. Key Eng Mater 2004;254–256:593–6.
[13] Ott CS, Development of bi-layer mineralized bone and cartilage regeneration template. M Eng Thesis, DMSE, MIT, 2005.
[14] Lynn AK, Bonfield W. A novel method for the simultaneous titrant-free control of pH and calcium phosphate mass yield. Acc Chem Rev 2005;38(3):202–7.
[15] Lynn AK, Cameron RE, Best SM, Brooks RA, Rushton N, Bonfield W. A novel design approach for the production of calcium phosphate–collagen biocomposites. Key Eng Mater 2004;254–256:593–6.
[16] Lynn AK, Best SM, Cameron RE, Harley BA, Yannas IV, Gibson LJ, Bonfield W. Design of a multiphase osteochondral scaffold II: control of chemical composition. J Biomed Mater Res (Part A), submitted for publication.
[17] Harley BA, Lynn AK, Wissner-Gross Z, Bonfield W, Yannas IV, Gibson LJ. Design of a multiphase osteochondral scaffold IV: fabrication of layered scaffolds with soft interfaces. J Biomed Mater Res (Part A), submitted for publication.
[18] Lynn AK, Brooks RA, Bonfield W, Rushton N. Repair of defects in articular joints: prospects for novel materials-based solutions in tissue engineering. J Bone Joint Surg (British Ed) 2004;84-B(8):1093–9.
[19] Currey JD. Bones – structure and mechanics. Princeton University Press; 2002.
[20] Martin RB, Burr DB, Sharkey NA. Skeletal tissue mechanics. New York: Springer; 1998.
[21] Yannas IV, Lee E, Orgill DP, Skrabut EM, Murphy GF. Synthesis and characterization of a model extracellular matrix that induces partial regeneration of adult mammalian skin. Proc Natl Acad Sci 1989;86:933–7.
[22] Yannas IV. Similarities and differences between induced organ regeneration in adults and early foetal regeneration. J Roy Soc Interf 2005;2:403–17.
[23] Spilker MH, Asano K, Yannas IV, Spector M. Contraction of collagen–glycosaminoglycan matrices by peripheral nerve cells in vitro. Biomaterials 2001;22:1085–93.
[24] Yannas IV, Burke JF, Gordon PL, Huang C, Rubenstein RH. Design of an artificial skin. II. Control of chemical composition. J Biomed Mater Res 1980;14:107–31.
[25] Yannas IV, Burke JF. Design of an artificial skin. I. Basic design principles. J Biomed Mater Res 1980;14:65–81.
[26] Hollinger JO, Einhorn TA, Doll BA, Sfeir C. Bone tissue engineering. Boca Raton, FL: CRC Press; 2005.
[27] Harley BA, Leung JH, Silva ECCM, Gibson LJ. Mechanical characterization of a homologous series of equiaxed collagen–GAG scaffolds. Acta Biomater 2007;3:463–74.
[28] Harley BA, Flemings MC. Coarsening-mediated solidification is responsible for defining the pore microstructure of collagen–

glycosaminoglycan scaffolds: experimental and thermal modeling results. Acta Mater, in press.
[29] O'Brien FJ, Harley BA, Yannas IV, Gibson LJ. The effect of pore size on cell adhesion in collagen–GAG scaffolds. Biomaterials 2005;26:433–41.
[30] Gibson LJ. Biomechanics of cellular solids. J Biomech 2005;38:377–99.
[31] O'Brien FJ, Harley BA, Yannas IV, Gibson LJ. Influence of freezing rate on pore structure in freeze-dried collagen–GAG scaffolds. Biomaterials 2004;25:1077–86.
[32] Dagalakis N, Flink J, Stasikelis P, Burke JF, Yannas IV. Design of an artificial skin. Part III. Control of pore structure. J Biomed Mater Res 1980;14:511–28.
[33] Kim HW, Knowles JC, Kim HE. Hydroxyapatite and gelatin composite foams processed via novel freeze-drying and crosslinking for use as temporary hard tissue scaffolds. J Biomed Mater Res, Part A 2005;72A:136–45.
[34] Tadic D, Beckmann F, Schwarz K, Epple M. A novel method to produce hydroxyapatite objects with interconnecting porosity that avoids sintering. Biomaterials 2004;25:3335–40.
[35] Salgado AJ, Figueiredo JE, Coutinho OP, Reis RL. Biological response to pre-mineralized starch based scaffolds for bone tissue engineering. J Mater Sci: Mater Med 2005;16:267–75.
[36] Pan SX, Li Y, Feng HL, Bai W, Gu YY. In vitro aging of mineralized collagen-based composite as guided tissue regeneration membrane. Mater Sci Eng C 2006;26:724–9.
[37] Wang FM, Qiu K, Hu T, Wan CX, Zhou XD, Gutmann JL. Biodegradable porous calcium polyphosphate scaffolds for the three-dimensional culture of dental pulp cells. Int Endod J 2006;39:477–83.
[38] Munar ML, Udoh K, Ishikawa K, Matsuya S, Nakagawa M. Effects of sintering temperature over 1300 degrees C on the physical and compositional properties of porous hydroxyapatite foam. Dental Mater J 2006;25(1):51–8.
[39] Reis RL, Cunha AM, Fernandes MH, Correia RN. Treatments to induce the nucleation and growth of apatite-like layers on polymeric surfaces and foams. J Mater Sci: Mater Med 1997;8:897–905.
[40] Zou C et al. Preparation and characterization of porous beta-tricalcium phosphate/collagen composites with an integrated structure. Biomaterials 2005;26:5276–84.
[41] Tanahashi M, Yao T, Kokubo T, Minoda M, Miyamoto T, Nakamura T, Yamamuro T. Apatite coating on organic polymers by a biometric approach. J Am Ceram Soc 1994;77(11):2805–8.
[42] Oliveira AL, Malafaya PB, Reis RL. Sodium silicate gel as a precursor for the in vitro nucleation and growth of a bone-like apatite coating in compact and porous polymeric structures. Biomaterials 2003;24:2575–84.
[43] Zhang Y, Zhang M. Synthesis and characterization of macroporous chitosan/calcium phosphate composite scaffolds for tissue engineering. J Biomed Mater Res 2001;55(3):304–12.
[44] Hing KA, Gibson IR, Revell PA, Best SM, Bonfield W. Influence of phase purity on the in vivo response to hydroxyapatite. Bioceramics 2000:373–6.
[45] Kikuchi M, Itoh S, Ichinose S, Shinomiya K, Tanaka J. Self-organization mechanism in a bone-like hydroxyapatite/collagen nanocomposite synthesized in vitro and its biological reaction in vivo. Biomaterials 2001;22:1705–11.
[46] Rhee SH, Suetsugu Y, Tanaka J. Biomimetic configurational arrays of hydroxyapatite nanocrystals on bio-organics. Biomaterials 2001;22:2843–7.
[47] Jenkins R, Snyder RL. Introduction to X-ray powder diffractometry. New York, NY: John Wiley & Sons; 1996.
[48] Klug HP, Alexander LE. X-ray diffraction procedures: for polycrystalline and amorphous materials. 2nd edition. New York, NY: John Wiley & Sons; 1974.
[49] Silva E, Van Vliet KJ. Robust approach to maximize the range and accuracy of force application in atomic force microscopes with nonlinear position-sensitive detectors. Nanotechnology 2006;17:5525–30.
[50] Silva E, Tong L, Yip S, Van Vliet KJ. Size effects on the stiffness of silica nanowires. Small 2006;2(2):239–43.
[51] Chiang CY, Mello CM, Gu J, Silva E, Van Vliet KJ, Belcher AM. Weaving genetically engineered functionality into mechanically robust virus fibers. Adv Mater 2007;19:826–32.
[52] VanLandingham MR. Review of instrumented indentation. J Res Natl Ins Std Technol 2003;108(4):249–65.
[53] Schuh CA. Nanoindentation studies of materials. Mater Today 2006;9(5):32–40.
[54] Oliver WC, Pharr GM. Measurement of hardness and elastic modulus by instrumented indentation: advances in understanding and refinements to methodology. J Mater Res 2004;19(1):3–20.
[55] Yannas IV, Tobolsky AV. Cross linking of gelatin by dehydration. Nature 1967;215:509–10.
[56] Beevers CA. The crystal structure of dicalcium phosphate dihydrate, $CaHPO_4 \cdot 2H_2O$. Acta Crystallogr 1957;11:273–7.
[57] MacLeenan G, Beevers CA. The crystal structure of dicalcium phosphate, $CaHPO_4$. Acta Crystallogr 1955;8:579–83.
[58] Babis GC, Soucacos PN. Bone scaffolds: the role of mechanical stability and instrumentation. Injury–Int J Care Inj 2005;36S:S38–44.
[59] Jones JR, Hench LL. Regeneration of trabecular bone using porous ceramics. Curr Opin Solid State Mater Sci 2003;7:301–7.
[60] Karageorgiou V, Kaplan D. Porosity of 3D biomaterial scaffolds and osteogenesis. Biomaterials 2005;26:5474–91.
[61] Zhang SM, Cui FZ, Liao SS, Zhu Y, Han L. Synthesis and biocompatibility of porous nano-hydroxyapatite/collagen/alginate composite. J Mater Sci: Mater Med 2003;14:641–5.
[62] Yin Y, Ye F, Cui J, Zhang F, Li X, Yao K. Preparation and characterization of macroporous chitosan–gelatin/beta-tricalcium phosphate composite scaffolds for bone tissue engineering. J Biomed Mater Res A 2003;67(3):844–55.
[63] Heughebaert JC, Lebugle A, Vu F, Phan-Tan-Luu R. Central composite design and optimization by multiresponse analysis of octacalcium phosphate synthesis. Analysis 2000;28:571–4.
[64] Brown WE, Smith JP, Lehr JR, Frazier AW. Octacalcium phosphate and hydroxyapatite: crystallographic and chemical relations between octacalcium phosphate and hydroxyapatite. Nature 1962;196:1048–55.
[65] Raatikainen P, Silvennoinen R, Ketolainen J, Ketolainen P, Paronen P. Evaluation of pharmaceutical beam bending tests using double-exposure holographic interferometry. Eur J Pharm Biopharm 1997;44:261–7.
[66] Vajjhala S, Kraynik AM, Gibson LJ. A cellular solid model for modulus reduction due to resorption of trabeculae in bone. J Biomech Eng 2000;122:511–5.
[67] Guo XE, Kim CH. Effects of age-related bone loss: a 3D microstructural simulation. In: Proc. 1999 bioengineering conference, ASME, vol. 42; 1999. p. 327–8.
[68] Silva MJ, Gibson LJ. The effect of non-periodic microstructure and defects on the compressive strength of two-dimensional cellular solids. Int J Mech Sci 1997;39(5):549–63.
[69] Silva MJ, Hayes WC, Gibson LJ. The effect of non-periodic microstructure on the elastic properties of two-dimensional cellular solids. Int J Mech Sci 1995;37(11):1161–77.
[70] Wahl DA, Sachlos E, Liu C, Czernuszka JT. Controlling the processing of collagen–hydroxyapatite scaffolds for bone tissue engineering. J Mater Sci: Mater Med 2007;18:201–9.
[71] Yunoki S, Ikoma T, Monkawa A, Ohta K, Kikuchi M, Sotome S, Shinomiya K, Tanaka J. Control of pore structure and mechanical property in hydroxyapatite/collagen composite using unidirectional ice growth. Materials letters. 60 (2006) 999-1002.